RSC Advances

PAPER

View Article Online
View Journal | View Issue

Cite this: *RSC Adv.*, 2021, **11**, 8228

Green sol–gel auto combustion synthesis and characterization of double perovskite Tb_2ZnMnO_6 nanoparticles and a brief study of photocatalytic activity

Mina Dara,[a] Mohammad Hassanpour,[a] Hassan Abbas Alshamsi,[b] Mahin Baladi[a] and Masoud Salavati-Niasari *[a]

In this work, new double perovskite Tb_2ZnMnO_6 nanoparticles were successfully synthesized by a sol–gel auto combustion method. To synthesize these nanoparticles, three known sugars, lactose, fructose, and maltose, and liquorice powder, which contains quantities of sugar and other organic compounds, were used as fuel. Images obtained from Scanning Electron Microscopy (SEM) analysis implied that maltose-based nanoparticles are homogenous and less in particle size. Further, different maltose ratios were applied to get the best size and morphology. The optimum sample was used to continue the other analysis to check other features of the nanoparticles. Also, the optimum sample was used for the removal of dye contamination under the photocatalytic process. Photocatalytic tests were performed in neutral and alkaline pH conditions under UV-light irradiation. It has been found that the decolorization percent for methyl orange was about 35% and for methyl violet about 55% at neutral pH. Also, this value for methyl violet was about 90% at pH = 8. The results obtained from the study of photocatalytic properties introduce these nanoparticles as a desirable option for removing dye contaminants from aqueous media.

Received 10th December 2020
Accepted 15th February 2021

DOI: 10.1039/d0ra10400k

rsc.li/rsc-advances

1. Introduction

Due to the increase in pollution, and incredibly polluted water resources, access to safe water has become one of the major human activities in the present age.[1] Also, existing organic compounds from industrial wastewater in water sources are a concern for human health.[2] Different methods have been employed to remove water pollution and for wastewater treatment. For example, coagulation–flocculation, chemical precipitation, ion exchange, adsorption, membrane filtration, electrochemical treatments and photocatalytic methods can be mentioned.[3–9] One of the green and useful procedures is using nanoparticles under the photocatalytic process.[10,11] Many parameters affect the photocatalytic properties of materials, such as the amount of catalyst,[12] active sites,[13] the specific surface area of the catalyst,[14] the desired contamination concentration,[15] and the pH of the environment.[16] However, the main feature of materials to study their application in the photocatalytic process is their optical and electronic properties.[17] In the photocatalytic process, the unique electronic and optical properties of the nanoparticles can be lead to a production electron–hole pair and consequently increasing the free radicals. Produced free radicals could destroy organic contamination.[18,19] With their attractive physical and chemical properties, the perovskites materials are a proper candidate for the photocatalyst process.[20]

Perovskites are a large family of materials with unique and broad properties. In the meantime, double perovskites with the Re_2ABO_6 formula (that Re is the rare earth and A and B are transition metal) are of great interest because of their electronic structure and unique features, including magnetic, dielectric, magneto-dielectric, and magneto-caloric.[21–23] It should be noted that the cation capacity and oxygen vacancy concentration play an essential role in the physical and electrochemical properties of these perovskites.[24] Various applications have been reported for double perovskites, including solar cell,[25] capacitors and piezoelectric,[26] anti-counterfeiting labels,[27] anode materials for solid oxide fuel cells,[28] oxygen carrier,[29] water splitting,[30] catalysts[31] and photocatalyst.[32] Single perovskites have long been considered an active catalyst. As a subset of the perovskite family, double perovskites are evolving options that can compete with single perovskites.[33]

Employing double perovskites in the photocatalytic process had many reports in the literature. For example, Shirazi *et al.* synthesized La_2MnTiO_6 double perovskite nanostructures using a simple sol–gel method in the presence of citric acid. They

[a]*Institute of Nano Science and Nano Technology, University of Kashan, P. O. Box 87317-51167, Kashan, Iran. E-mail: Salavati@kashanu.ac.ir; Fax: +98 31 55913201; Tel: +98 31 5591 2383*

[b]*Department of Chemistry, College of Education, University of Al-Qadisiyah, Diwaniya 1753, Iraq*

utilized photocatalytic properties of the nanoparticles to remove the acid blue dye and reported 72% degradation under visible irradiation.[34] Li *et al.* prepared Ca_2NiWO_6 by the solid-state method and used these double perovskites for the generation H_2 and O_2 in the photocatalytic process under visible light irradiation. The decrease in photocatalytic activity because of the oxygen vacancies in the compound, which acts as the electron–hole recombination centre.[35] In another report, Hu *et al.* investigated the photocatalytic properties of La_2FeTiO_6 for *p*-chlorophenol degradation under visible light. They showed that the photocatalytic activity of La_2FeTiO_6 under visible light was superior to that of $LaFeO_3$.[36] According to the results of these reports, the photocatalytic properties of these nanoparticles can be recorded as one of the attractive and widely used properties for these nanoparticles.

There are several methods for preparing double perovskites, such as solvothermal,[37] sol–gel technique,[38] solid-state,[26] microwave-assisted combustion.[29] In this study, the synthesis of double perovskite of Tb_2ZnMnO_6 nanoparticles for the first time was reported. The nanoparticles were prepared by sol–gel auto combustion using several sugars as fuel. The nanoparticles were analyzed for size and morphology as well as purity. Because of the optical and electrical properties of these nanoparticles, the photocatalyst test was performed against two dye solutions, containing methyl orange and methyl violet under UV light.

2. Experimental

2.1. Materials and characterization

All the materials used in this work except liquorice were commercially available and employed without further purification. $Tb(NO_3)_3\cdot 6H_2O$ with a molecular weight of 453.03 g mol^{-1}, $Mn(NO_3)_2\cdot 4H_2O$ with a molecular weight of 251.01 g mol^{-1}, $Zn(NO_3)_2\cdot 6H_2O$ with a molecular weight of 297.49 g mol^{-1} with a purity of over 99% were purchased from Merck company. XRD (X-ray diffraction) patterns were collected from a diffractometer of the Philips Company with X'PertPro monochromatized Cu Kα radiation (λ = 1.54 Å). The microscopic morphology of the products was studied by FESEM (Field Emission Scanning Electron Microscopy) (Mira3 Tescan) and TEM (Transmission Electron Microscopy) (HT-7700). EDS (Energy Dispersive Spectrometry) analysis was studied by XL30, Philips microscope. Magnetic properties were measured using VSM (vibrating sample magnetometer) (Meghnatis. Daghigh Kavir Co.; Kashan Kavir; Iran). The N_2 adsorption/desorption analysis (BET) was performed at −196 °C using an automated gas adsorption analyzer (Tristar 3000, Micromeritics).

2.2. Synthesis route

Tb_2ZnMnO_6 double perovskite nanoparticles were synthesized by sol–gel auto combustion method. In the beginning, transparent solutions containing 2 mmol of $Tb(NO_3)_3\cdot 6H_2O$, 1 mmol of $Zn(NO_3)_2\cdot 6H_2O$, and 1 mmol of $Mn(NO_3)_2\cdot 4H_2O$ was prepared in distilled water separately. An aqueous solution containing 2 mmol maltose was also prepared simultaneously. Afterward, the maltose solution was added dropwise to the solution containing terbium ions under magnetic stirring at room temperature (S1). The zinc solution was then added to the manganese solution (S2). After 5 minutes of stirring, the S2 solution was added to the S1 solution which containing terbium and maltose. The obtained solution was then homogenized for 50 minutes at 50 °C on the stirrer. Then the temperature was raised to 110 °C, and after 30 minutes by evaporation of the solvent, a soft powder was obtained. The resulting powder was dried in an oven at 80 °C. The powder was then calcined for five hours at 900 °C. Other conditions were applied to examine the particle size and morphology listed in Table 1.

2.3. Preparation for photocatalytic tests

The photocatalytic performance of Tb_2ZnMnO_6 nanoparticles was explored by the degradation of methyl orange and methyl violet as organic pollutants under UV irradiation. The decolorization reactions were done in a quartz photocatalytic reactor. 0.05 g of the as-synthesized Tb_2ZnMnO_6 nanoparticles were mixed as a photocatalyst in 100 ml of dye solution at a concentration of 5 ppm. This mixture was aerated for 30 min to reach adsorption equilibrium in a dark room. After that, the solution was exposed to UV-light. The photocatalytic tests were done at room temperature. Samples are taken at the appropriate time and analyzed by UV-vis spectrometer. The degradation percent was calculated as follows:

$$\%\ \text{decolorization} = (A_0 - A_t)/A_0 \times 100$$

where A_0 and A_t are the absorbance value of dye solution at 0 and t min, respectively.[16]

The effect of pH was also investigated as one of the factors affecting the photocatalytic activity of nanoparticles by adjusting the pH to 8 for methyl violet dye. 10 ppm for methyl violet

Table 1 Different conditions of synthesis procedure

No.	Mole ratio of Tb : Zn : Mn	Fuel	Ratio of fuel to Tb	Calcination temperature °C
1	2 : 1 : 1	Lactose	1 : 1	900
2	2 : 1 : 1	Fructose	1 : 1	900
3	2 : 1 : 1	Maltose	1 : 1	900
4	2 : 1 : 1	Liquorice	0.5 g powder	900
5	2 : 1 : 1	Liquorice	0.5 g powder	800
6	2 : 1 : 1	Maltose	1 : 2	900
7	2 : 1 : 1	Maltose	3 : 2	900

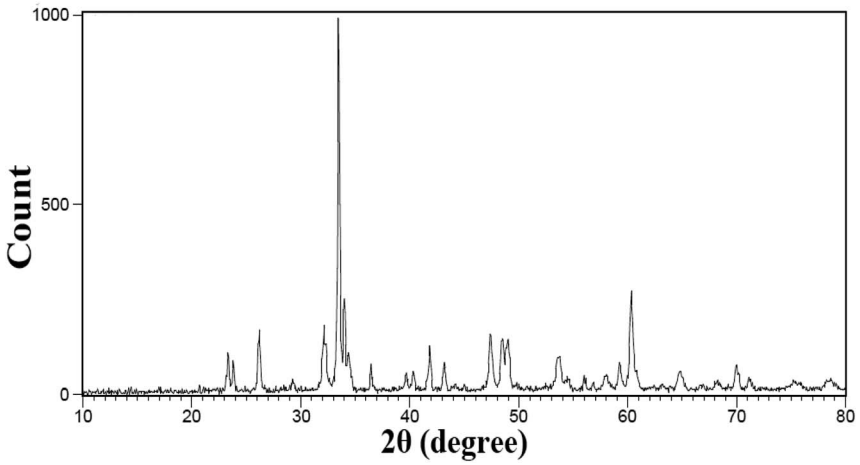

Fig. 1 XRD pattern of sample no. 3.

(as higher concentration) and 2.5 ppm for methyl orange (as lower concentration) were prepared and used to investigate the effect of dye concentration on photocatalytic activity.

3. Result and discussion

Because this compound was synthesized for the first time, there is no reference pattern to compare with the pattern obtained from that. Hence, the diffraction pattern obtained was compared with the diffraction pattern of the possible side metal oxide products. Given that there is no evidence of the formation of side metal oxide products, this pattern is introduced as the double perovskite pattern of Tb_2ZnMnO_6, as can be seen in Fig. 1. By comparing the XRD pattern obtained with other patterns reported such as Gd_2CoMnO_6,[39] Tb_2NiMnO_6,[40] and Dy_2CoMnO_6,[41] many similarities are observed which confirm the formation of the product. To confirm these observations, the reference peaks of the Gd_2CoMnO_6 compound (JCPDS = 01-085-0960) was showed with the pattern obtained sample no. 2 in Fig. 2. Crystallite size was obtained for the product (sample no. 4) of 33 nm using XRD pattern data and the Scherrer equation.[16]

The XRD pattern of sample no. 5, which was calcined at 800 °C, is shown in Fig. 3(a). As can be seen, the peak of the TbO_2 index is exactly above 29 degrees, which decreased sharply with increasing temperature to about 900 °C in the other samples. As a result, growing the temperature enhances the purity of the compound. One possible mechanism for the synthesis of this product could be related to the formation of separate metal oxides of the present compounds before calcination and the subsequent arrival of the final product after calcination. Fig. 3(b and c) shows the X-ray patterns of samples no. 6 and 7, which synthesized with the molar ratio of (b) 1 : 2 and (c) 3 : 2 of maltose to terbium precursor. The calculated crystallite size is 35 and 31 nm, respectively.

Different fuels in the synthesis pathway of Tb_2ZnMnO_6 nanoparticles can lead to studying particle morphology, homogeneity, and size. Fuels release heat, carbon dioxide, and water during the combustion process and homogenize the solution by forming complexes with metal ions. Formation of fuel complex with ions in the first step transforms the fuel as a capping agent to prevent the ions from reacting and forming by-products. The type of fuel also affects combustion

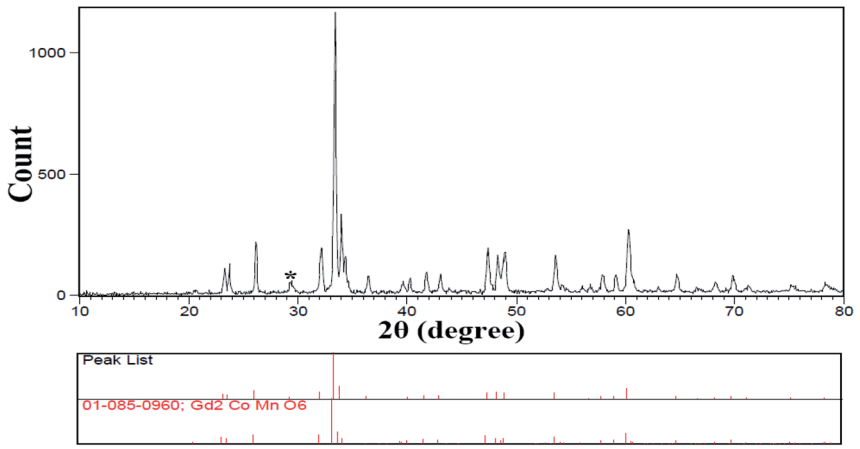

Fig. 2 XRD pattern of sample that used fructose as fuel sample no. 2.

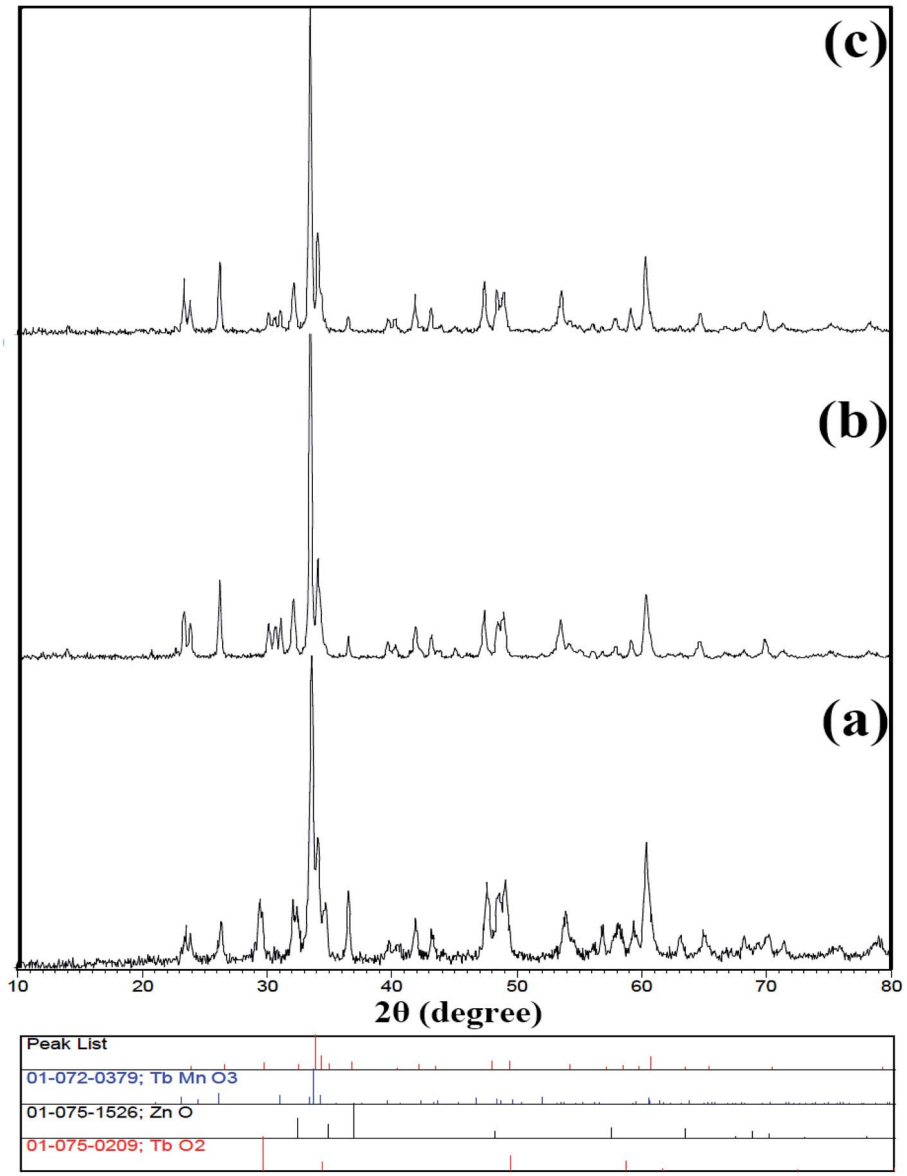

Fig. 3 XRD pattern of (a) sample no. 5 (b) sample no. 6 and (c) sample no. 7.

intensity, and proper combustion leads to better results and sometimes better purity.[42,43] The surface morphology and size of prepared nanoparticles were first analyzed by SEM analysis. In Fig. 4(a–h), SEM images of nanoparticles synthesized with different fuels are presented at two magnifications (Sample no. 1–4).

Due to the high calcination temperature and high reactivity of the nanoparticles, particles were agglomerated, and the particle size was relatively large. However, in a partial examination of the histogram (Fig. 5(a–d)), the particle size distribution in sample no. 3 that used maltose as a fuel showed a higher percentage of particle size than the rest of the samples below 100 nm. When the images were magnified, this claim is closer to the truth that particles in sample no. 3 are more uniform than in the other samples. Fig. 4(g and h) illustrates the sample synthesized in the presence of Liquorice as fuel. Although the particles have a particular shape, they are larger than the other samples, and in Fig. 4(h) (1 μm scale image), the particle aggregation is quite clear.

Two different molar ratios of terbium to maltose were applied to obtain nanoparticles with smaller size. Fig. 6(a–d) shows SEM images of nanoparticles synthesized at different molar ratios using maltose. As can be seen from the images, the nanoparticles were arranged sequentially as chains. It is clear that when the highest amount of maltose was used, the particles have a better morphology and structure (Fig. 6(c and d)). In Fig. 7, the histogram of the particle size distribution for these two samples is plotted. What comes out of the details of the histogram diagram is confirmation of selecting the sample containing the most amount of maltose as the optimal sample. The TEM analysis was applied for sample no. 7 to analyze the particle size and morphology more thoroughly. As shown in Fig. 8, relatively spherical particles with sizes 30 to 40 nm are stuck together.

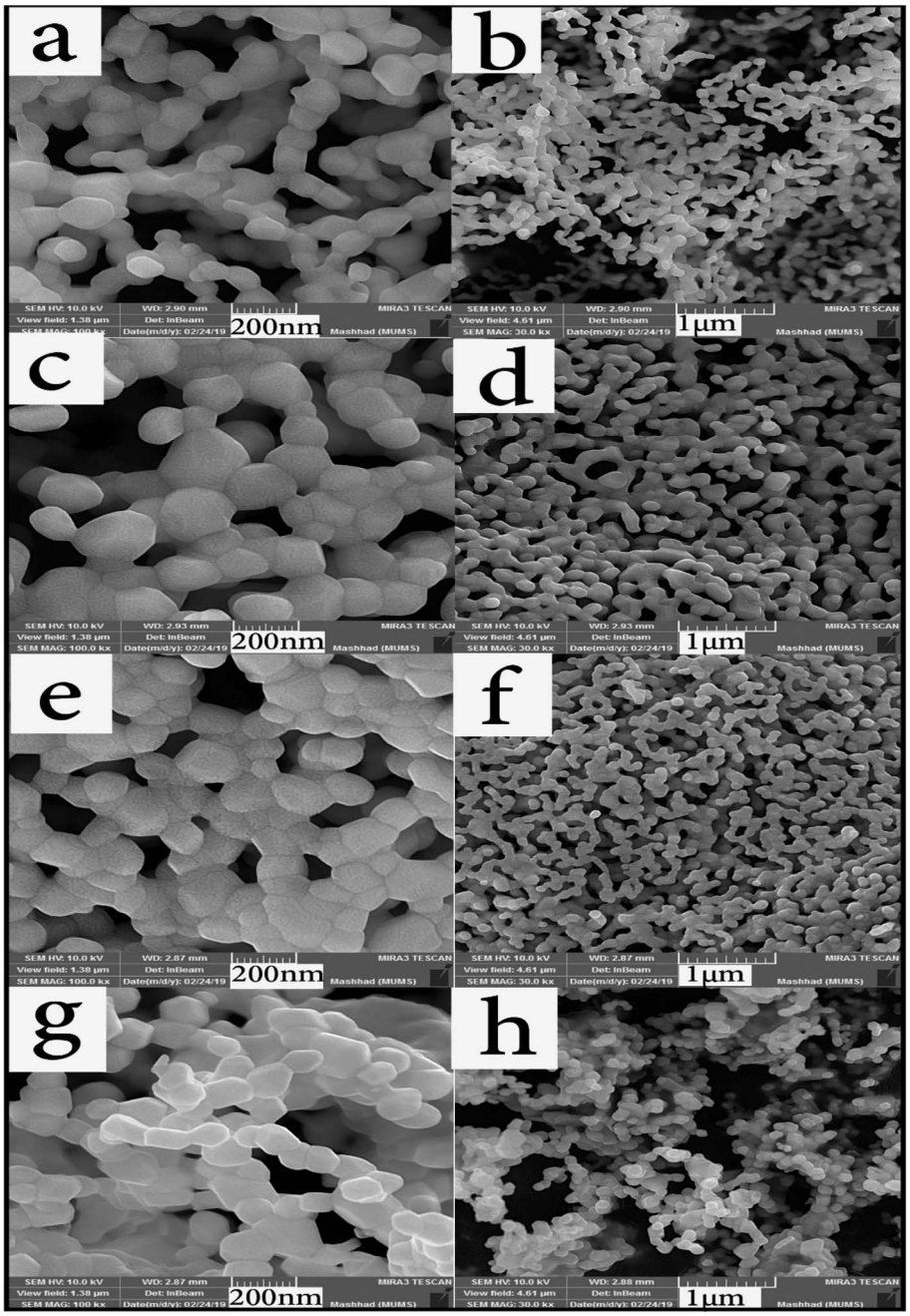

Fig. 4 SEM images of samples prepared with different fuels, (a and b) lactose, (c and d) fructose, (e and f) maltose, and (g and h) liquorice.

FT-IR analysis is used to investigate the functional groups of organic compounds further. Fig. 9 shows the FT-IR spectra of the Tb_2ZnMnO_6 nanoparticles prepared in the presence of maltose as fuel (sample no. 7). The absorption peaks at 3451 and 1628 cm^{-1} are attributed to the moisture on the surface of the Tb_2ZnMnO_6 sample.[16] The absorption bands at about 605 and 463 cm^{-1} are assigned to metal–oxygen bonds, which can be related to Mn–O and Zn–O, respectively. The EDS analysis was applied for sample no. 7 (Fig. 10) to confirm the purity of the synthesized nanoparticles. The EDS analysis reveals that the elements in the product are Tb, Mn, Zn, and O. Considering the values of 20, 10, 10, and 60% of Tb, Zn, Mn, and O elements in Tb_2ZnMnO_6 structure and considering the quantitative inaccuracy of EDS analysis, comparing these values with the results obtained from EDS analysis confirms the formation of these nanoparticles. The approximate EDS calculations give the product $Tb_{1.5}Zn_{0.5}Mn_{0.5}\ O_{7.5}$.

The magnetic properties of Tb_2ZnMnO_6 nanoparticles were evaluated at 300 K. According to the graph obtained from VMS analysis (Fig. 11(a)), the paramagnetic behavior can be considered for these nanoparticles. The magnetic behavior of the nanoparticles used in the photocatalyst process is an advantage because of their easy recycling.[44]

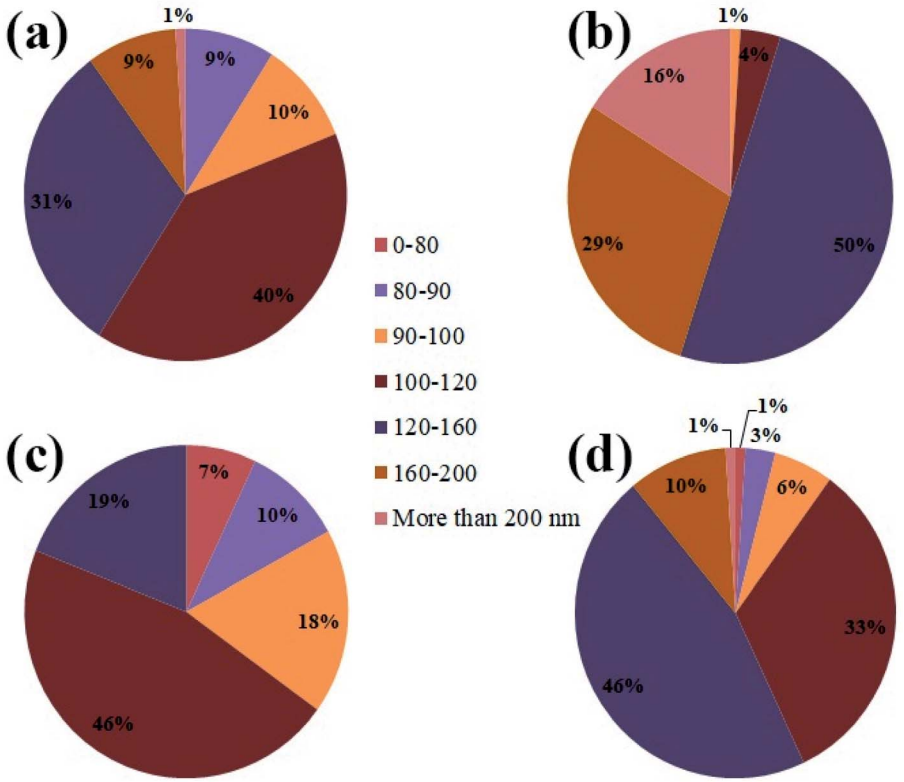

Fig. 5 The histogram graph of the particle size distribution from sample no. 1–4, (a) lactose, (b) fructose, (c) maltose, and (d) liquorice.

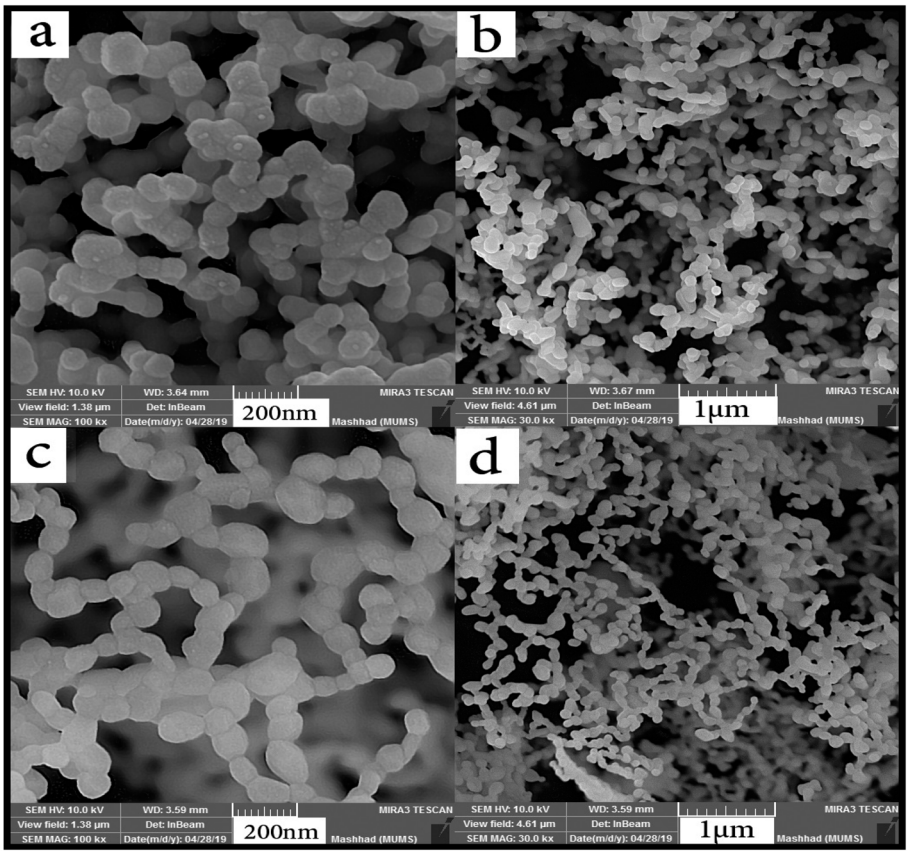

Fig. 6 SEM images of the effect of maltose content on the size and morphology of Tb_2ZnMnO_6 nanoparticles, (a and b) sample no. 6 and (c and d) sample no. 7.

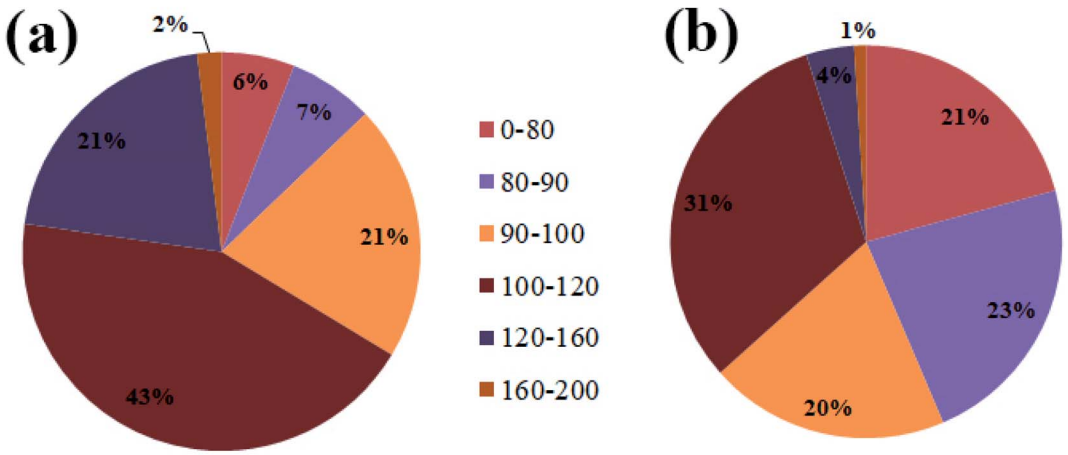

Fig. 7 The histogram graph of the particle size distribution from sample no. (a) 6, (b) 7.

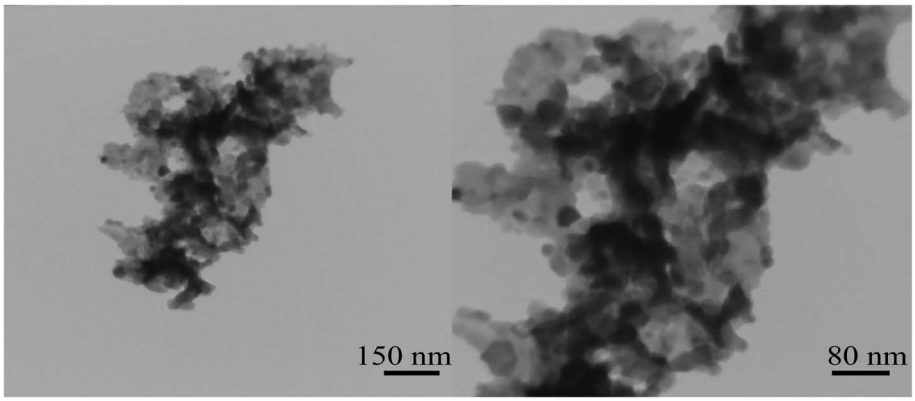

Fig. 8 TEM image of Tb_2ZnMnO_6 nanoparticles sample no. 7.

The DRS analysis was used to identify the optical properties of the synthesized nanoparticles, and the results can be seen in Fig. 11(b). The spectra obtained from DRS analysis was used to calculate the band-gap, which is an essential operative for the photocatalyst process. The band-gap was calculated from the Tauc's equation.[45] The optical energy band-gap of the nanoparticles was defined using the following relation:

$$(\alpha h\nu)^n = C(h\nu - E_g)$$

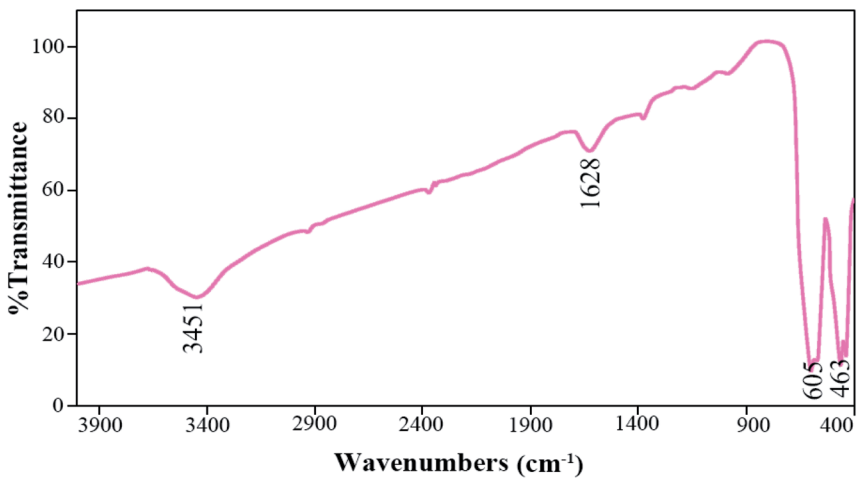

Fig. 9 FT-IR of as-synthesized nanoparticles after calcination at 900 °C sample no. 7.

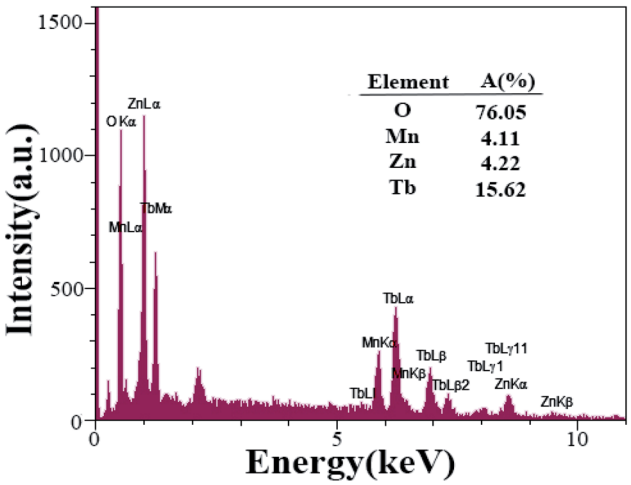

Fig. 10 EDS spectra of Tb_2ZnMnO_6 nanoparticles sample no. 7.

where $h\nu$ is the photo energy, α is the absorption coefficient, C is a constant relative to the material, and n is either 2 for a direct transition or 1/2 for an indirect transition.

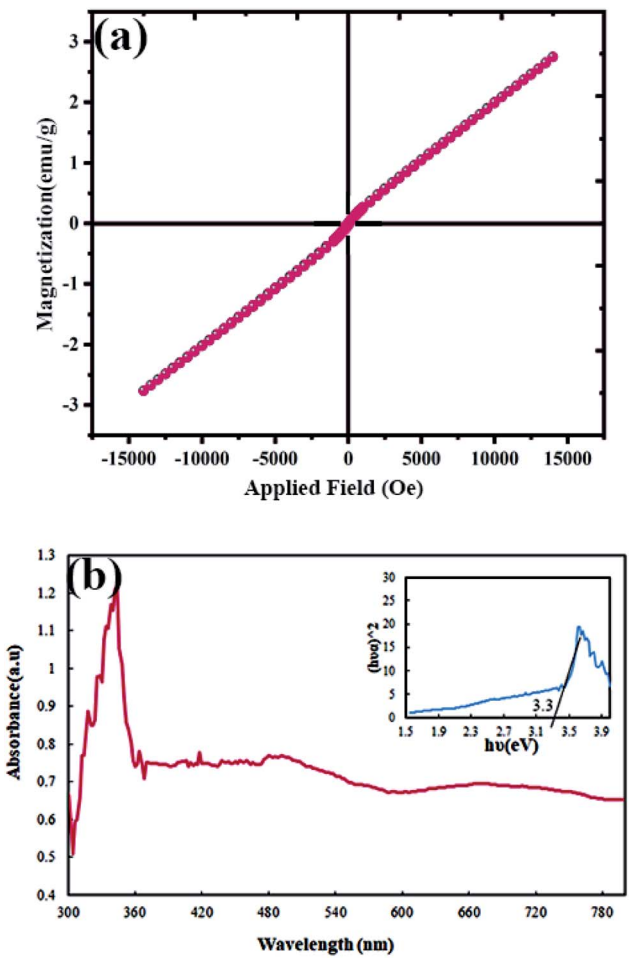

Fig. 11 (a) Magnetization *versus* applied magnetic field at room temperature and (b) diffuse reflectance spectra (DRS) of Tb_2ZnMnO_6 nanoparticles sample no. 7.

BET calculation was performed to estimate surface area and pore volume in the structure synthesized by nitrogen adsorption/desorption isotherms measured at 77 K. Fig. 12(a) and (b) shows adsorption/desorption isotherms and BJH plots of Tb_2ZnMnO_6 nanoparticles, respectively. As is clear from the figure, the type III isotherm with a type H3 hysteresis loop for Tb_2ZnMnO_6 nanoparticles was obtained from the BET method. The specific surface areas, total pore volumes, and mean pore diameters obtained from the BET were 6.7316 ($m^2\ g^{-1}$), 0.016529 ($cm^3\ g^{-1}$), and 9.8216 (nm), respectively.

The aqueous solutions containing methyl orange and methyl violet were used to evaluate the photocatalytic properties of Tb_2ZnMnO_6 nanoparticles. The simultaneous testing was performed on the nanoparticles under dark conditions to investigate the amount of dye absorption on the nanoparticles. The obtained results, along with the results of the BET analysis, indicates that the physical absorption at the nanoparticle surface has a negligible effect on the photocatalyst results. Subsequently, the samples were analyzed under UV light for 90 min. As shown in Fig. 13(a), after 90 min, the decolorization percent for the sample containing methyl orange and methyl violet was calculated 34% and 52%, respectively. Cationic dyes are preferred over negatively

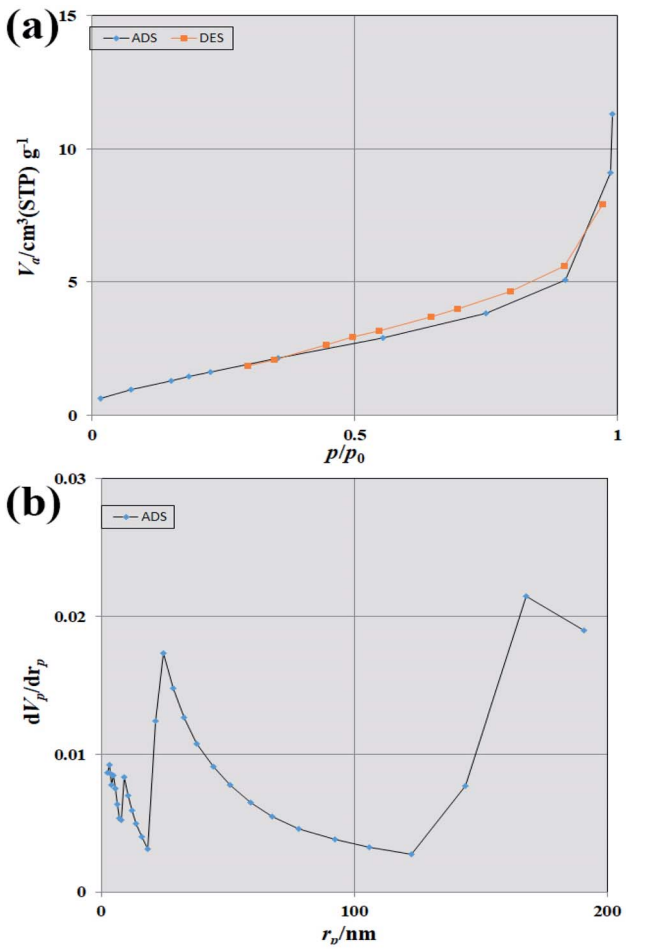

Fig. 12 (a) N_2 adsorption/desorption isotherms and (b) BJH pore size distributions of Tb_2ZnMnO_6 nanoparticles.

charged photocatalytic materials in alkaline media. Since methyl violet is a cationic dye, and also in alkaline environments, the surface of photocatalyst material is negatively charged, thus increasing the pH value, increases the dye contact with the nanoparticle, which promote the photocatalytic activity by electron transfer.[46–48] By considering these points, the photocatalytic test for the sample containing methyl violet was performed at pH = 8. After adjusting the pH, the photocatalytic test was performed for the sample containing methyl violet, and about 90% decolorization was obtained. The possible mechanism in the path of the photocatalyst process is as follows:

$$Tb_2ZnMnO_6 \text{ nanoparticles} + h\nu \rightarrow Tb_2ZnMnO_6 \text{ nanoparticles}^* + e^- + h^+$$

$$h^+ + H_2O \rightarrow H^+ + OH^\cdot$$

$$e^- + O_2 \rightarrow O_2^-$$

$$\text{Dye solution} + OH^\cdot + O_2^- \rightarrow \text{decolorization solution}$$

Although the decolorization percentage was not significant at neutral pH, by changing the pH and increasing the dye contact with the nanoparticles, an acceptable decolorization percentage was obtained for Tb_2ZnMnO_6 nanoparticles.

A concentration of 10 ppm of methyl violet (in pH = 8) and a concentration of 2.5 ppm of methyl orange was used to investigate the effect of dye concentration on the efficiency of the photocatalyst process (Fig. 13(b)). After performing the photocatalytic process, dye degradation was about 61% for methyl violet and 56% for methyl oranges. Increasing the concentration of dye and enhance their adsorption on the catalyst surface, reducing the absorption of OH and its conversion to hydroxyl radicals. The reduction of hydroxyl radicals is directly related to the decrease of photocatalytic efficiency. According to Beer–Lambert law, the path of the photons entering the solution is reduced, resulting in less photon absorption and reduced photocatalytic reaction rate.[49] Several results of the photocatalytic activity of other double perovskites are presented in Table 2 to compare the

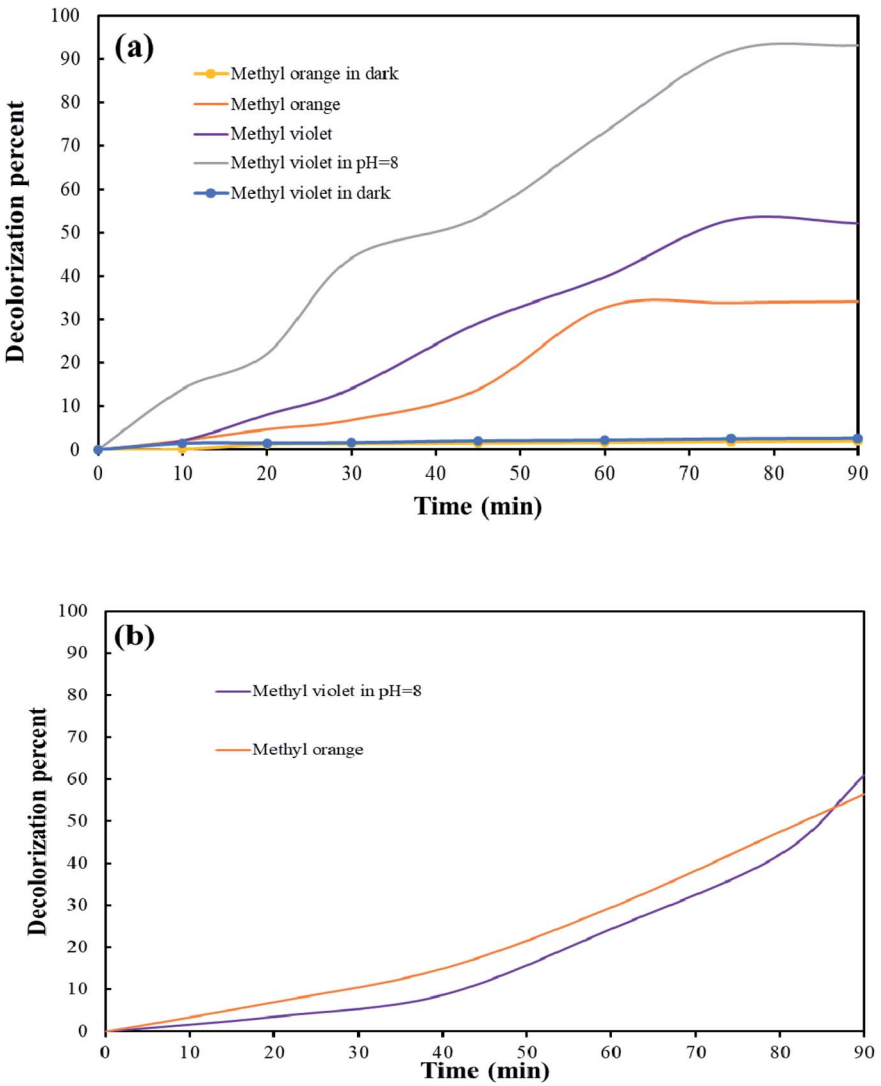

Fig. 13 Photocatalytic activity of Tb_2ZnMnO_6 nanoparticles on decolorization of methyl orange and methyl violet (a) dye concentration 5 ppm (b) dye concentration 10 and 2.5 ppm for methyl violet and methyl orange respectively.

Table 2 Photocatalytic activity of double perovskites for different dye

Double perovskites	Band-gap (eV)	Dye	Photocatalytic activity	Reference
$Cs_2AgBiBr_6$	2	Rhodamine b	98%	50
Dy_2ZnMnO_6	3.2	Methyl violet	90.44%	32
Sm_2NiMnO_6	1.41	Rhodamine b	87%	51
Gd_2CoMnO_6	3.2	Eriochrome black T	85%	52
La_2MnTiO_6	2.8	Acid blue 113	72%	34
Gd_2ZnMnO_6/ZnO	3.4	Methyl violet	60%	53
Tb_2ZnMnO_6	3.3	Methyl violet	90%	This work

photocatalytic activity of Tb_2ZnMnO_6 nanoparticles. As it is known, double perovskites are developing their application field in close competition with single perovskites as one of the most widely used structures.

4. Conclusion

In summary, the nanoparticles of Tb_2ZnMnO_6 double perovskites were successfully synthesized by the sol–gel auto combustion method *via* maltose, fructose, lactose, and liquorice powder as fuel. In the first step, the type of fuel was optimized considering the suitable size and morphology of the product obtained. Next, two molar ratios of optimum maltose fuel with terbium precursors were used for the synthesis. The optimum sample was selected after performing the relevant analyses. Ft-IR and EDS analyses were used to confirm the purity of the prepared particles. The band-gap was calculated at about 3.3 eV for Tb_2ZnMnO_6 double perovskites, which is a good value for the photocatalytic process. The photocatalytic activity of this nanoparticle was investigated in the presence of methyl orange and methyl violet as an organic dye. The photocatalytic test results under UV light for a sample containing methyl violet at alkaline pH showed 90% decolorization. The results of the BET analysis confirmed that this amount of decolorization was obtained only from the photocatalytic properties of these nanomaterials. The obtained results introduce Tb_2ZnMnO_6 double perovskites as a suitable candidate as a photocatalyst to remove organic dyes in effluents.

Conflicts of interest

There are no conflicts to declare.

Acknowledgements

Authors are grateful to the council of Iran National Science Foundation; INSF (97017837) and University of Kashan for supporting this work by Grant No (159271/009).

References

1 H. A. Hasan and M. H. Muhammad, *J. Water Process. Eng.*, 2020, **33**, 101035.
2 P. Chowdhary, R. N. Bharagava, S. Mishra and N. Khan, in *Environmental Concerns and Sustainable Development*, Springer, 2020, pp. 235–256.
3 M. Lv, Z. Zhang, J. Zeng, J. Liu, M. Sun, R. S. Yadav and Y. Feng, *Sep. Purif. Technol.*, 2019, **212**, 337–343.
4 X. Li, Q. Zhao and X. Hao, *J. Waste Manag.*, 1999, **19**, 409–415.
5 I. Levchuk, J. J. R. Màrquez and M. Sillanpää, *Chemosphere*, 2018, **192**, 90–104.
6 N. Jiang, R. Shang, S. G. Heijman and L. C. Rietveld, *Water Res.*, 2018, **144**, 145–161.
7 W. Song, Z. Li, Y. Ding, F. Liu, H. You, P. Qi, F. Wang, Y. Li and C. Jin, *Chem. Eng. J.*, 2018, **331**, 695–703.
8 B. P. Chaplin, *Acc. Chem. Res.*, 2019, **52**, 596–604.
9 R. Ameta, M. S. Solanki, S. Benjamin and S. C. Ameta, in *Advanced Oxidation Processes for Waste Water Treatment*, Elsevier, 2018, pp. 135–175.
10 K. Karthik, M. Shashank, V. Revathi and T. Tatarchuk, *Mol. Cryst. Liq. Cryst.*, 2018, **673**, 70–80.
11 J. Singh, S. Kumar, H. K. Verma and R. Soni, *Opt. Mater.*, 2020, **110**, 110506.
12 J. Kaur and S. Singhal, *Phys. B*, 2014, **450**, 49–53.
13 P. Wang, Y. Sheng, F. Wang and H. Yu, *Appl. Catal., B*, 2018, **220**, 561–569.
14 N. M. Flores, U. Pal, R. Galeazzi and A. Sandoval, *RSC Adv.*, 2014, **4**, 41099–41110.
15 J. Grzechulska and A. W. Morawski, *Appl. Catal., B*, 2002, **36**, 45–51.
16 M. Hassanpour, H. Safardoust-Hojaghan and M. Salavati-Niasari, *J. Mol. Liq.*, 2017, **229**, 293–299.
17 J. Singh, A. K. Manna and R. Soni, *J. Mater. Sci.*, 2019, **30**, 16478–16493.
18 J. Singh and R. Soni, *Colloids Surf.*, 2021, **612**, 126011.
19 J. Singh and R. Soni, *New J. Chem.*, 2020, **44**, 14936–14946.
20 J. Kong, T. Yang, Z. Rui and H. Ji, *Catal. Today*, 2019, **327**, 47–63.
21 M. Retuerto, A. Munoz, M. J. Martinez-Lope, J. A. Alonso, F. J. Mompean, M. T. Fernandez-Diaz and J. Sanchez-Benitez, *Inorg. Chem.*, 2015, **54**, 10890–10900.
22 H. J. Zhao, X. Q. Liu, X. M. Chen and L. Bellaiche, *Phys. Rev. B: Condens. Matter Mater. Phys.*, 2014, **90**, 195147.
23 L. Su, X.-Q. Zhang, Q.-Y. Dong, Y.-J. Ke, K.-Y. Hou, C.-S. Liu and Z.-H. Cheng, *J. Alloys Compd.*, 2018, **746**, 594–600.
24 Y. Huang, M. Karppinen, H. Yamauchi and J. B. Goodenough, *Phys. Rev. B: Condens. Matter Mater. Phys.*, 2006, **73**, 104408.
25 C. Wu, Q. Zhang, Y. Liu, W. Luo, X. Guo, Z. Huang, H. Ting, W. Sun, X. Zhong and S. Wei, *Adv Sci*, 2018, **5**, 1700759.
26 Y. Lin, X. Chen and X. Liu, *Solid State Commun.*, 2009, **149**, 784–787.

27 W. Hu, T. Li, X. Liu, D. Dastan, K. Ji and P. Zhao, *J. Alloys Compd.*, 2020, **818**, 152933.
28 Y.-H. Huang, G. Liang, M. Croft, M. Lehtimaki, M. Karppinen and J. B. Goodenough, *Chem. Mater.*, 2009, **21**, 2319–2326.
29 R. L. Medeiros, V. R. Melo, D. M. Melo, H. P. Macedo, G. T. Moure, I. Adánez-Rubio, M. A. Melo and J. Adánez, *Int. J. Hydrogen Energy*, 2020, **45**, 1681–1696.
30 J. Wang, Y. Gao, D. Chen, J. Liu, Z. Zhang, Z. Shao and F. Ciucci, *ACS Catal.*, 2018, **8**, 364–371.
31 R. Hu, R. Ding, J. Chen, J. Hu and Y. Zhang, *Catal. Commun.*, 2012, **21**, 38–41.
32 M. Baladi, F. Soofivand, M. Valian and M. Salavati-Niasari, *Ultrason. Sonochem.*, 2019, **57**, 172–184.
33 X. Xu, Y. Zhong and Z. Shao, *Trends Chem.*, 2019, **1**, 410–424.
34 P. Shirazi, M. Rahbar, M. Behpour and M. Ashrafi, *New J. Chem.*, 2020, **44**, 231–238.
35 D. Li, J. Zheng and Z. Zou, *J. Phys. Chem. Solids*, 2006, **67**, 801–806.
36 R. Hu, C. Li, X. Wang, Y. Sun, H. Jia, H. Su and Y. Zhang, *Catal. Commun.*, 2012, **29**, 35–39.
37 C. Singh, V. N. Thakur and A. Kumar, *Ceram. Int.*, 2021, **47**, 6982–6987.
38 R. N. Mahato, K. Sethupathi and V. Sankaranarayanan, *J. Appl. Phys.*, 2010, **107**, 09D714.
39 X. Wang, J. Horvat, H. Liu, A. Li and S. Dou, *Solid State Commun.*, 2001, **118**, 27–30.
40 M. Nasir, S. Kumar, N. Patra, D. Bhattacharya, S. N. Jha, D. R. Basaula, S. Bhatt, M. Khan, S.-W. Liu and S. Biring, *ACS Appl. Electron. Mater.*, 2019, **1**, 141–153.
41 M. Valian, F. Beshkar and M. Salavati-Niasari, *J. Mater. Sci.*, 2017, **28**, 12440–12447.
42 V. Bhagwat, A. V. Humbe, S. More and K. Jadhav, *Mater. Sci. Eng., B*, 2019, **248**, 114388.
43 F. Ansari, A. Sobhani and M. Salavati-Niasari, *J. Colloid Interface Sci.*, 2018, **514**, 723–732.
44 S. Huang, Y. Xu, M. Xie, H. Xu, M. He, J. Xia, L. Huang and H. Li, *Colloids Surf.*, 2015, **478**, 71–80.
45 J. Tauc, R. Grigorovici and A. Vancu, *Phys. Status Solidi B*, 1966, **15**, 627–637.
46 L. Bonetto, F. Ferrarini, C. De Marco, J. Crespo, R. Guégan and M. Giovanela, *J. Water Process. Eng.*, 2015, **6**, 11–20.
47 L. Zhu, P. Zhu, L. You and S. Li, *Clean Technol. Environ.*, 2019, **21**, 81–92.
48 A. F. Shojaei, A. R. Tabari and M. H. Loghmani, *Micro Nano Lett.*, 2013, **8**, 426–431.
49 E. Yassıtepe, H. Yatmaz, C. Öztürk, K. Öztürk and C. Duran, *J. Photochem. Photobiol., A*, 2008, **198**, 1–6.
50 Z. Zhang, Y. Liang, H. Huang, X. Liu, Q. Li, L. Chen and D. Xu, *Angew. Chem., Int. Ed.*, 2019, **58**, 7263–7267.
51 M. S. Sheikh, A. P. Sakhya, R. Maity, A. Dutta and T. Sinha, *Sol. Energy Mater. Sol. Cells*, 2019, **193**, 206–213.
52 R. Mohassel, A. Sobhani, M. Salavati-Niasari and M. Goudarzi, *Spectrochim. Acta, Part A*, 2018, **204**, 232–240.
53 Y. Orooji, R. Mohassel, O. Amiri, A. Sobhani and M. Salavati-Niasari, *J. Alloys Compd.*, 2020, 155240.